Chapter 8

The Proximity Effect

In studies of the redshift distribution of Ly α clouds described by equation (7.4), it was noticed early on (Carswell et al. 1982) that the γ values determined from individual QSOs were lower than those obtained by considering the line counts from several or many QSOs collectively. Murdoch et al. (1986) called this countervailing trend in the spectra of individual QSOs the "inverse effect" and showed that it resulted at least in part from including the region within roughly 4 Mpc of the quasar, which seemed to have a lower number density than regions in the spectrum that were further shortward of Ly α emission. They suggested that the effect was due to the radiation field of the quasar, which increased the degree of ionization of nearby hydrogen clouds and led to correspondingly lower column densities of neutral hydrogen.

Other, alternative explanations for the inverse effect were discussed (e.g., by Tytler 1987), but none found wide acceptance. For example, one suggestion was that the size of Ly α clouds in general means that clouds close to a quasar were too small to completely cover the quasar's emission-line region, so that the absorption falling within the Ly α emission line would show lower equivalent widths than similar clouds further from the quasar. But studies of common absorption lines in the images of gravitationally lensed quasars and in close QSO pairs indicate sizes on the scale of hundreds of kiloparsecs (e.g., Smette et al. 1995), while the equivalent width distribution of Ly α forest lines on the broad wings of the Ly α emission line appears to be statistically the same as that of the lines in the QSO continuum (Lu, Wolfe and Turnshek 1991).

8.1 The Photoionization Model

Bajtlik, Duncan and Ostriker (1988) were the first to present a quantitative physical model to explain the inverse effect, which they referred to as the "proximity effect." Providing a concrete model made it possible for the first time to use an independent method to infer the amount of photons coming from a metagalactic ultraviolet (UV) background at high redshifts.

First, the authors make the reasonable assumption that the Ly α clouds are highly ionized by the general background of UV photons, so that the neutral hydrogen density in a cloud will be inversely proportional to the radiation incident at frequencies greater than or equal to the Lyman limit.[1] Initially this means that in the sole presence of background radiation $J(\nu)$, which is normally given in units of erg cm^{-2} s^{-1} Hz^{-1} sr^{-1}, the H I column density of a cloud would be

$$N_{\mathrm{HI}} = \frac{N}{\int\limits_{\nu_{LL}}^{\infty} 4\pi J(\nu)} \tag{8.1}$$

If a bright quasar is also present, with a flux density of $F_Q(\nu)$ erg cm^{-2} s^{-1} Hz^{-1}, then the cloud's column density would drop to

$$N_{\mathrm{HI}} = \frac{N}{\int\limits_{\nu_{LL}}^{\infty} [F_Q(\nu) + 4\pi J(\nu)]} \tag{8.2}$$

where N is some hypothetical column density in both cases.

What seems to be the key assumption made by Bajtlik, Duncan and Ostriker at this point is that the frequency dependence of the background radiation above the Lyman limit is the same as that of the QSO radiation. In that case, the ratio of ionization rates will be equal to the ratio

$$\omega = \frac{F_{\nu_{LL}}}{4\pi J_\nu(z)} \tag{8.3}$$

of the Lyman-limit flux densities, where $J_\nu(z)$ is the Lyman-limit background intensity and $F_{\nu_{LL}}$ is the Lyman-limit flux density from the quasar, both at the location of the cloud. The column density for a cloud in the vicinity of a bright quasar then becomes

$$N_{\mathrm{HI}} = \frac{N_o}{1+\omega}\,, \tag{8.4}$$

where N_o would have been the column density in the absence of the quasar.

8.2 Luminosity Distance and Fluxes

In order to apply the ionization model to the Monte Carlo simulations presented below, it was necessary to estimate the Lyman-limit flux density of the quasar radiation coming from HE 0940. The principal task of the next two sections will be to explain how this was done. A few definitions and elementary calculations will be introduced here before the actual determination is described in section 8.3.

In static Euclidean space, the observed bolometric flux f (energy per unit area and time) is a function of the source's bolometric luminosity L (energy per unit time) and the distance r from the source:

$$f = \frac{L}{4\pi r^2} \tag{8.5}$$

[1] The Lyman limit corresponds to ionization energy for the hydrogen 1s state, which is 911.75 Å in wavelength terms.

Although this relation does not hold in expanding or curved space, it is used to define the luminosity distance d_L, which can be thought of as the distance the source would have from the observer if equation (8.5) were valid.

$$d_L \equiv \sqrt{\frac{L}{4\pi f}} \tag{8.6}$$

Kayser, Helbig and Schramm (1997) have presented a useful summary of the variously defined cosmological distances between two objects, expressing them in terms of the two redshifts, the Hubble constant H_o, the cosmological constant Λ_o, the density parameter Ω_o and the inhomogeneity parameter η (which is the fraction of homogeneously distributed matter in the Universe, as opposed to matter distributed in "clumps" on the scale of the distances being examined). The derivations of these expressions are complicated and some require numerical integration, but in the special case of $\Lambda_o = 0$, $\eta = 1$ and $\Omega_o > 0$ the luminosity distance can be given analytically:

$$d_L(z_x, z_y) = \frac{2c}{H_o}\frac{1}{{\Omega_o}^2}\frac{1}{(1+z_x)^3}\;[\,s(z_y)\cdot t(z_x) - s(z_x)\cdot t(z_y)\,] \tag{8.7}$$

$$\text{with} \quad \begin{aligned} s(z) &= \Omega_o z - \Omega_o + 2 \\ t(z) &= \sqrt{\Omega_o z + 1} \end{aligned}$$

Now it should be noted that equation (8.6) applies to bolometric fluxes f and luminosities L, in which the energy is integrated over all wavelengths or frequencies. Spectroscopic measurements, however, can deliver only (for example) the flux f_ν per unit frequency, usually in units of erg cm^{-2} s^{-1} Hz^{-1}. The quasar flux density $F_{\nu_{LL}}$ is also such a quantity. It is therefore necessary to know how its Lyman-limit flux at the cloud can be obtained in terms of the observed quasar flux at Earth. Because no publications could be found to explain this simple derivation, it is presented here.

Given a quasar with emission redshift z_Q, whose observed spectral flux $f_{\nu_{obs}}$ in erg cm^{-2} s^{-1} Hz^{-1} is measured at the frequency ν_{obs} at Earth. Then the intrinsic QSO luminosity in erg s^{-1} Hz^{-1} at the frequency $\nu_Q = \nu_{obs}\,(1+z_Q)$ is

$$L_{\nu_Q} = \frac{4\pi {r_Q}^2 f_{\nu_{obs}}}{1+z_Q} \tag{8.8}$$

where r_Q is the luminosity distance from Earth to the quasar, and the factor $1+z_Q$ is the bandwidth correction to account for the fact that the frequency interval observed at Earth is $d\nu_{obs} = d\nu_Q/(1+z_Q)$ (Weedman 1986).

Now suppose there is a cloud at redshift z_{cloud} with $0 \le z_{cloud} \le z_Q$. The local Lyman-limit flux $F_{\nu_{LL}}$ from the quasar, i.e., that seen at the frequency ν_{LL} in the cloud frame, is due to the luminosity at a higher frequency ν_Q in the quasar frame:

$$\nu_Q = \nu_{LL}\,\frac{1+z_Q}{1+z_{cloud}} \tag{8.9}$$

Writing equation (8.8) in the form

$$f_{\nu_{obs}} = \frac{L_{\nu_Q}}{4\pi {r_{_Q}}^2} \frac{\nu_{_Q}}{\nu_{obs}} \tag{8.10}$$

and applying it to the cloud frame, we obtain

$$F_{\nu_{_{LL}}} = \frac{L_{\nu_Q}}{4\pi {r_{_L}}^2} \left(\frac{1+z_{_Q}}{1+z_{cloud}} \right), \tag{8.11}$$

where the luminosity distance $r_{_L}$ is now the distance from the cloud to the quasar. Combining equations (8.8) and (8.11) yields the expression

$$F_{\nu_{_{LL}}} = \frac{f_{\nu_{obs}}}{1+z_{cloud}} \left(\frac{r_{_Q}}{r_{_L}} \right)^2 \tag{8.12}$$

where $\nu_{obs} = \nu_{_{LL}}/(1+z_{cloud})$. This, together with equation (8.7) for $r_{_Q}$ and $r_{_L}$, expresses the Lyman-limit flux at the cloud in terms of known quantities—namely the observed flux on Earth and the redshifts of the cloud and the quasar. The result is conveniently independent of the value of the Hubble parameter H_o.

8.3 Continuum Extrapolation

After deriving equation (8.12), the next step was to determine the absolute observed flux $f_{\nu_{obs}}$ from HE 0940. Because the narrow slit width used for the high-resolution echelle spectrum involves a very significant loss of light, absolute spectrophotometric data for HE 0940 had to be sought elsewhere.

Although Reimers et al. (1996) caution that the data from the Hamburg/ESO Survey should not be considered spectrophotometric, there are several reasons to believe that the exposures taken with the 1.52-meter telescope (Fig. 2.1) offer a very good estimate of the absolute spectral flux nonetheless. First of all, the observing conditions for these exposures were good. Secondly, all of the HES spectra were corrected for atmospheric extinction, and the accuracy of the flux calibration is estimated to be better than 20% for most of them. And finally, in the case of HE 0940, simulations of the B-band photometry for the 1.52-meter spectrum are in very good agreement with the measured CCD B magnitude cited in section 2.1 as well as with two separate determinations of the photographic B magnitude that were also available. For these reasons, the flux values can be considered relatively reliable down to about 4000 Å (L. Wisotzki, private communication).

Once this was established, the available flux f_λ in erg cm^{-2} s^{-1} Å^{-1} had to be converted into the flux f_ν in erg cm^{-2} s^{-1} Hz^{-1}. Then, in order to compute the quasar's Lyman-limit flux at a given absorber, it was necessary to determine the intrinsic quasar luminosity at correspondingly higher frequencies (this, often together with the bandwidth correction, is known as the K-correction).

The first step is easily accomplished by considering the energy emitted in the spectral interval $d\lambda$ around any given wavelength λ. If f_λ is the flux per unit wavelength there, and f_ν is the flux per unit frequency in the corresponding frequency interval $d\nu$, then $f_\lambda\, d\lambda = -f_\nu\, d\nu$ because the emitted energy is the same in both cases. The two quantities are related by

$$f_\nu = -f_\lambda \frac{d\lambda}{d\nu} = -f_\lambda \frac{d}{d\nu}\left(\frac{c}{\nu}\right) = \frac{\lambda^2}{c} f_\lambda \tag{8.13}$$

The second step requires additional work because the available spectrum does not cover the relevant wavelength region below the Lyman limit, which would have appeared at 3700 Å. The flux values were therefore extrapolated to those wavelengths by assuming that the quasar continuum can be parametrized by a power law. This common assumption usually takes the form

$$L_\nu \propto \nu^\alpha \tag{8.14}$$

for the intrinsic luminosity L_ν emitted at frequency ν, but the same applies for the flux density f_ν as well:

$$f_\nu \propto \nu^\alpha \tag{8.15}$$

In both cases, the exponent α is assumed to be constant for the quasar or at least for the spectral region under consideration. Common values for the power law in this form are $-1.0 \lesssim \alpha \lesssim -0.5$. Equation (8.13) yields the corresponding wavelength dependence:

$$f_\lambda \propto \lambda^{-(2+\alpha)} \tag{8.16}$$

This shows that the known flux density at a particular wavelength λ_{ref} suffices to calculate the flux density at any other wavelength λ_{obs}:

$$f_{\lambda_{obs}} = f_{\lambda_{ref}} \left(\frac{\lambda_{ref}}{\lambda_{obs}}\right)^{2+\alpha} \tag{8.17}$$

The problem then becomes one of determining the parameter α for the quasar at hand.

This was done by fitting the power law in equation (8.16) to the continuum in the 1.52-meter spectrum. Avoiding absorption lines as well as the broader emission lines, several segments redward of Ly α emission were chosen manually and flagged as belonging to the continuum. Since the coefficient and exponent in a power-law fit will vary drastically depending on their mutual values, some non-linear fitting methods yielded different results for different initial values or even failed to converge. The simplest alternative in this case was to take the natural logarithm

$$\ln f_\lambda = -(2+\alpha)\ln\lambda + \text{const.} \tag{8.18}$$

of both sides of equation (8.17), plot the quantity $y = \ln f_\lambda$ as a function of $x = \ln\lambda$, and fit a straight line through the 104 selected data points. The errors $\sigma_y = \sigma_f / f_\lambda$ in the data points were determined from the flux errors at each point using error propagation. The resulting linear least-squares fit and the corresponding continuum fit are shown in Figure 8.1. The slope $m = -(2+\alpha)$ of the fit yielded a power-law index of $\alpha = -1.06 \pm 0.03$. Of course the quoted error is not very meaningful, since the greater uncertainty comes from the choice of continuum points.

Given the power-law index, all that was needed was a reference wavelength and the flux density there. The flux $f_{\lambda_{ref}} = 6.18 \times 10^{-16}$ erg cm^{-2} s^{-1} Å^{-1} at $\lambda_{ref} = 6756.39$ Å was chosen because it was located away from prominent absorption or emission, in a region where the power-law fit deviated least from the measured fluxes. This allowed a determination of the emitted quasar flux, and hence the intrinsic luminosity, at any wavelength for which the power-law approximation was valid.

For example, with equations (8.8), (8.7), (8.13) and (8.17), the intrinsic Lyman-limit luminosity of HE 0940 was estimated to be

$$L_{\nu_{LL}} = \frac{4\pi {r_Q}^2}{1+z_Q} \frac{{\lambda_{obs}}^2}{c} f_{\lambda_{ref}} \left(\frac{\lambda_{ref}}{\lambda_{obs}}\right)^{2+\alpha} = 2.2 \times 10^{31} h^{-2} \text{ erg s}^{-1} \text{ Hz}^{-1} \tag{8.19}$$

for $H_o = 100h$ km s^{-1} Mpc^{-1} and $\Omega_o = 1$. In this particular case, λ_{obs} is the observed wavelength of the Lyman limit, 911.75 Å $(1+z_Q)$. Similarly, with the help of equations (8.14) and (8.9), equation (8.12) becomes

$$F_{\nu_{LL}} = \frac{L_{\nu_{LL}}}{4\pi {r_L}^2} \left(\frac{1+z_Q}{1+z_{cloud}}\right)^{\alpha} \tag{8.20}$$

where r_L is again the luminosity distance from the cloud to the quasar as given by equation (8.7). These equations are another way of expressing the relation in equation (8.12), which was used as the basis for the Monte Carlo calculations of the proximity effect.

8.4 Monte Carlo Methods

Generally speaking, Monte Carlo calculations refer to statistical methods of studying problems based on the use of random numbers (Bevington and Robinson 1992). This was the approach used to generate simulated data with random redshifts and column densities drawn from the non-uniform distributions in equations (7.4) and (7.5). Most random-number generators produce normalized uniform deviates, so that any number between 0 and 1 is equally probable. The computational problem, then, was to convert such uniformly distributed numbers into non-uniform distributions in the form of power laws.

Lyons (1986) has a very understandable description of three different Monte Carlo methods for generating non-uniform distributions, and summarizes their advantages and disadvantages. In terms of efficiency and computer time, the so-called transformation method used below is preferable to the rejection method or to weighting each

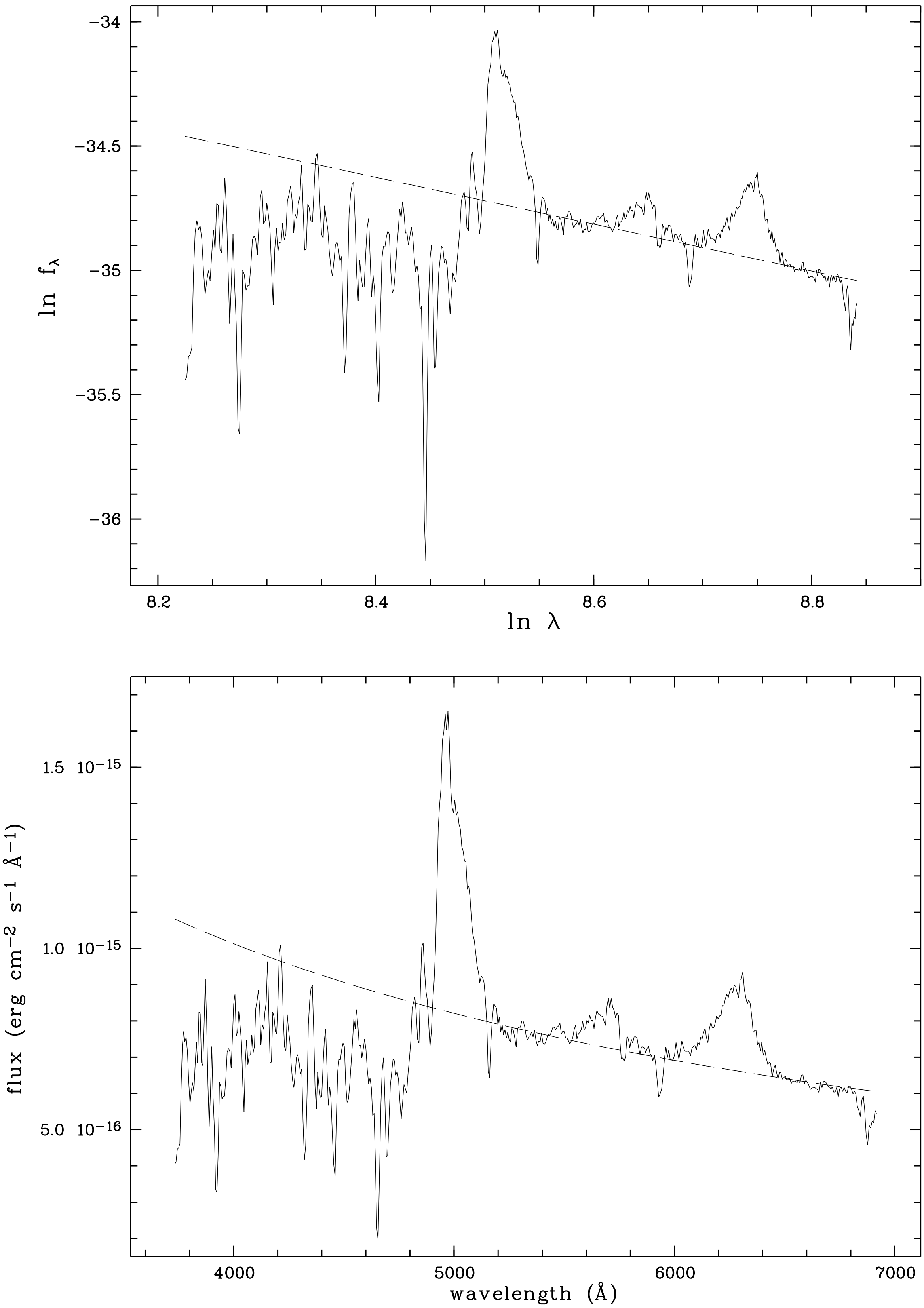

Figure 8.1: *Extrapolation of HE 0940–1050 continuum in 1.52-meter spectrum. TOP PANEL: Linear least-squares fit on logarithmic scale. BOTTOM PANEL: Resulting continuum fit in wavelength space.*

point. The transformation method can only be applied if the function involved can be integrated and then inverted, as was the case here.

Lyons explains that if we transform a variable x with a uniform distribution to $y = y(x)$, the distribution in y will generally not remain uniform. Therefore, to produce a specified non-uniform distribution $y(x)$, the problem is to find the correct transformation.

Given a random variable x, let the probability of generating a value between x and $x + dx$ be $p(x)\,dx$, whose the integral over x is normalized to 1, as is usual for probabilities. For example, for the uniform deviates $x \in (0, 1)$ provided by most computer algorithms,

$$p(x)\,dx = \begin{cases} dx & \text{for } 0 < x < 1 \\ 0 & \text{otherwise} \end{cases} \tag{8.21}$$

and the normalization is

$$\int_{-\infty}^{\infty} p(x)\,dx = \int_0^1 p(x)\,dx = \int_0^1 dx = 1 \tag{8.22}$$

Given a second random variable $y = y(x)$, with probability distribution $p(y)$. Because these are probabilities, $|p(x)\,dx| = |p(y)\,dy|$ and $f(y) = p(y)$ is a positive function whose integral is 1. Then

$$f(y) = \left| p(x)\,\frac{dx}{dy} \right| = \left| \frac{dx}{dy} \right| \tag{8.23}$$

Solving the differential equation yields the relation between x and y:

$$x = \int_0^y f(y')\,dy' =: F(y) \tag{8.24}$$

But the real goal is to obtain y as a function of x. If the function F is invertible, the transformation which takes a uniform deviate x into one distributed as $f(y)$ is

$$y(x) = F^{-1}(x) \tag{8.25}$$

Now the equations above (from Press 1992) assume that $y \in (0, 1)$. If y has a different domain, namely $y \in (y_{min}, y_{max})$, then the properly normalized function is

$$F(y) = \frac{\int_{y_{min}}^{y} p(y')\,dy'}{\int_{y_{min}}^{y_{max}} p(y')\,dy'} \tag{8.26}$$

In the present case of a power-law probability distribution $p(y) = y^a$ with $a \neq -1$, equation (8.24) becomes

$$x = F(y) = \frac{\int_{y_{min}}^{y} y^a \, dy}{\int_{y_{min}}^{y_{max}} y^a \, dy} = \frac{y^{\,1+a} - y_{min}^{\,1+a}}{y_{max}^{\,1+a} - y_{min}^{\,1+a}} \tag{8.27}$$

so the desired relation is

$$y = F^{-1}(x) = \left[y_{min}^{\,1+a} + x \left(y_{max}^{\,1+a} - y_{min}^{\,1+a} \right) \right]^{\frac{1}{1+a}} \tag{8.28}$$

Thus, to obtain a random redshift or column-density value drawn from the correct distribution, all that was necessary was to take the random value between 0 and 1 provided by the computer and apply equation (8.28) using the substitutions below.

$$\begin{array}{lcccccc} \text{For the } z \text{ distribution:} & y & \rightarrow & 1+z, & a & \rightarrow & \gamma \\ \text{For the } N_{\rm HI} \text{ distribution:} & y & \rightarrow & -\beta, & a & \rightarrow & N_{\rm HI} \end{array} \tag{8.29}$$

8.5 Monte Carlo Programs

The simulated data sample was composed of 10,000 simulations each for models A1 and A3 of Fardal, Giroux and Shull (1998). Each simulation was a "line list" in which each line was represented by a redshift value z and a column-density value $N_{\rm HI}$. The input to the program which produced these simulations was the model number (A1 or A3), the redshift range $[z_{min}, z_{max}]$, and the minimum and maximum allowed column densities $[N_{min}, N_{max}]$ for the lines to be created.

Normally, the Monte Carlo algorithm derived in the previous section would have enabled a computer program to do a simulation by merely calculating the total number of absorbers predicted by the model, choosing the actual total for the simulation from a Poisson distribution around the predicted total, and drawing random z and $N_{\rm HI}$ values from the appropriate distributions for all of the lines in the simulation. However, as can be seen in Table 7.1, the parameters in models A1 and A3 took on different values in different column-density regions, so these regions had to be handled separately.

The presence of distinct column-density regions required an additional three steps at the beginning of each group of 10,000 simulations:

1. Depending on the model chosen, the boundaries of the column-density regions and the parameter values $\mathcal{A}_o$, β and γ for those regions were stored in an array for easy access.[2]

[2] Note that since the models had been scaled to fit the data, the $\mathcal{A}_o$ values for model A1 were 1.32 times higher, and the $\mathcal{A}_o$ values for model A3 were 1.36 times higher, than those listed in Table 7.1.

2. If the input range $[N_{min}, N_{max}]$ covered more than one column-density region in the given model, it was broken up into smaller intervals whose boundaries matched those of the model regions.

3. For each of these smaller column-density intervals, the appropriate $\mathcal{A}_o$, β and γ values were read from the parameter array. The scaled model prediction for each column-density interval i was determined by integrating equation (7.6) to get

$$\mathcal{N}_{exp,i} = \frac{\mathcal{A}_o}{(1-\beta)(1+\gamma)} \left(z_{max}^{1+\gamma} - z_{min}^{1+\gamma}\right) \left[N_{min,i}^{1-\beta} - N_{max,i}^{1-\beta}\right] \tag{8.30}$$

where $\mathcal{N}_{exp,i}$ is the number of absorbers with $N_{min,i} \leq N_{\rm HI} \leq N_{max,i}$ expected to be found along the entire line of sight between z_{min} and z_{max}.

Although models A1 and A3 predicted the total number of absorbers $\mathcal{N}_{exp} = \sum \mathcal{N}_{exp,i}$ that would be found in the specified redshift range $[z_{min}, z_{max}]$ and column-density range $[N_{min}, N_{max}]$, of course the *actual* number of absorbers in each simulation varied. They were determined as follows:

4. In each simulation, the algorithm looped through each of the column-density intervals one by one.

5. The actual number of absorbers $\mathcal{N}_i$ in each column-density interval i was determined by using an algorithm from Press et al. (1992) to draw a random number from a Poisson distribution around the mean $\mathcal{N}_{exp,i}$.

6. Each one of the $\mathcal{N}_i$ absorbers in the interval was assigned a redshift z and column density $N_{\rm HI}$ drawn randomly from distributions (7.4) and (7.5), respectively, with the help of equations (8.28) and (8.29).

7. After going through all of the column-density regions in the simulation, the data for the $\mathcal{N}_{total} = \sum \mathcal{N}_i$ lines in the simulation were written to disk in the form of $(z, N_{\rm HI})$ doublets.

8. Steps 4 to 6 were repeated 10,000 times.

The redshift range chosen for the simulations was $z \in (2.0, 3.068)$, and the column-density range was $\log N_{\rm HI} \in (12.5, 19.0)$. The lower column-density limit was chosen to match the lowest common detection limit in the spectrum, while the upper limit was chosen to be substantially higher than the $\log N_{\rm HI} = 17.0$ cut-off in the data sample to avoid depopulating that region when the ionizing flux from the quasar and the UVB were taken into account. The ranges in z and $N_{\rm HI}$ were also wider than those of the data in order to allow for some flexibility in the comparisons.

After the basic "unperturbed" simulations had been generated, other programs could be used to access the data pairs stored on disk and simulate the effects of ionizing radiation from a nearby quasar and the UV background.

1. For each absorber in a given simulation, the ionizing radiation from the quasar at z_{abs} was calculated using equation (8.12).

2. The UV background at $z = z_{abs}$ was either taken to be a constant or calculated using Model I of Bajtlik, Duncan and Ostriker (1988),

$$J_\nu(z) = j_\nu\,(1+z)^{3.5}\left[(1+z_{on})^{1.2} - (1+z)^{1.2}\right] \tag{8.31}$$

   where $j_\nu = 8.17 \times 10^{-24}$ erg cm^{-2} s^{-1} Hz^{-1} sr^{-1} (see section 8.6).

3. The column density of the absorber was then reduced according to equations (8.4) and (8.3). If the resulting column density dropped below the specified lower limit, the line was dropped from the sample.

4. The redshift distribution of the remaining sample was examined to see how well it compared to the actual distribution observed in the data.

The results of such comparisons are presented in the next section.

8.6 Comparisons to Models

The aim of this section is to look for evidence of a proximity effect in the spectrum of HE 0940–1050. The most effective way to do this is to plot the number of observed lines $\mathcal{N}$ as a function of the redshift, and to see if there are less lines close to the quasar redshift than are predicted by the scaled versions of models A1 and A3 of Fardal, Giroux and Shull.

As mentioned earlier, specific intervals in $N_{\rm HI}$ and z must be chosen in order to evaluate the integral in equation (7.6) and obtain concrete line counts. The choice of the largest interval in $N_{\rm HI}$ is clear, since the full data sample already has the range $13.33 \le \log N_{\rm HI} \le 17.0$. But since the simulations by Dobrzycki and Bechtold (1991b) indicate that the number counts of weak lines may be more strongly affected by quasar radiation, it will also be interesting to see if there is a dependence on column density. Therefore the data sample has also been divided up into a subsample of 114 "weak" lines with $13.33 \le \log N_{\rm HI} \le 14.0$, and a subsample of 55 "strong" lines with $14.0 \le \log N_{\rm HI} \le 17.0$. It was not possible to study smaller column-density intervals because of the already very poor statistics; for example, there were only 7 lines with $\log N_{\rm HI} \in [15.0, 16.0]$ and only 3 lines with $\log N_{\rm HI} \in [16.0, 17.0]$.

The comparisons between the simulations and the data are presented as plots of $\log(d\,\mathcal{N}\,/dz)$ vs. $\log(1+z)$. This form was chosen because taking the logarithm of both sides of equation (7.4) yields

$$\log \frac{d\mathcal{N}}{dz} = \gamma\ \log(1+z) + \log A_o \tag{8.32}$$

bin	from $\log(1+z)$	to $\log(1+z)$	z_{min}	z_{max}	λ_{min}	λ_{max}
1	0.534100	0.537884	2.420565	2.450514	4158.3	4194.7
2	0.537884	0.544884	2.450514	2.506580	4194.7	4262.8
3	0.544884	0.551884	2.506580	2.563557	4262.8	4332.1
4	0.551884	0.558884	2.563557	2.621460	4332.1	4402.5
5	0.558884	0.565884	2.621460	2.680304	4402.5	4474.0
6	0.565884	0.572884	2.680304	2.740105	4474.0	4546.7
7	0.572884	0.579884	2.740105	2.800876	4546.7	4620.6
8	0.579884	0.586884	2.800876	2.862636	4620.6	4695.7
9	0.586884	0.593884	2.862636	2.925398	4695.7	4772.0
10	0.593884	0.600884	2.925398	2.989181	4772.0	4849.5
11	0.600884	0.607884	2.989181	3.054000	4849.5	4928.3

Table 8.1: *Bins chosen for plots of* $\log(d\mathcal{N}/dz)$ *vs.* $\log(1+z)$.

which is a straight line in the variables $y = \log(d\mathcal{N}/dz)$ and $x = \log(1+z)$, making it easier to visually compare the data with the models. A bin size of 0.007 in $\log(1+z)$ was chosen for all the plots that will be presented here, though the redshift cut-off at the Ly β emission line makes the lowest bin only about half this size (0.003786). The bin entries were calculated by counting the number of lines $\mathcal{N}$ in each bin and dividing by the total redshift interval Δz covered by the bin, minus any gaps in redshift. The logarithm of the result was then plotted on the yaxis. Thus both the smaller bin size and the two regions excluded in section 7.4 were taken into account.

The disadvantage of this choice of representation is that the z values are not immediately evident. To facilitate comparisons between the plots here and the spectrum in Appendix B, the bin boundaries in both z and λ are listed in Table 8.1.

The calculations for the Monte Carlo simulations of models A1 and A3, both with and without ionizing radiation, were done in the same way—except that after the bin counts for the 10,000 simulations had been determined they were averaged for direct comparison to the data.

Forest models and photoionization model

In all of the figures that follow, the data points remain the same and the various models are shown as dashed or dotted lines which also indicate the size of the bins. Figure 8.2 shows the data with the scaled model predictions in the absence of quasar radiation. Even before the proximity-effect simulations are introduced, a few features seem obvious.

- The fit for the data sample as a whole, in the top plot, is generally good; except in the first and last bins, it falls almost completely within range of the (Poissonian,

$1\,\sigma$) error bars of the data. The two bins closest to the quasar seem to indicate a possible proximity effect.

- In the weak-line sample, the fit is also generally good, though the first two bins lie above, and the fifth bin lies well below, the model predictions. The strong drop in number counts in the bin closest to the quasar is even more pronounced in the weak-line sample than in the sample as a whole.

- The fit is generally not quite as good for the strongest lines as in the other two cases. Any proximity effect that might be present in the last two bins is much smaller than the deviations elsewhere, most notably in the three consecutive bins that lie clearly below the model predictions. This may be the result of the poorer statistics for this subsample; for example, the three low redshift intervals contain only 3 entries each.

Figure 8.3 shows the fits that result when the column densities in the simulations are reduced using the photoionization model and a particular model for the UVB background presented by Bajtlik, Duncan and Ostriker (1988). Their Model I was obtained by integrating a luminosity function and extrapolating to higher redshifts. When determining the integrated background radiation, it assumes that all quasars turn "on" at $z_{on} = 4$. It also assumes $\Omega_o = 1$, so this was the value adopted for all of the calculations and plots in this section as well.

The ionization model fits the data well, yielding an especially good fit for the full sample, falling within the error bars of all but the high first bin, and hitting the value in the last bin almost exactly. The fit for the weaker lines is also good, although it looks like the proximity effect for those lines is probably even stronger. The fit for the strongest lines, on the other hand, offers only a very slight improvement over the models without radiation, and this seems to be primarily because the fit happens to fall above and below the last two bin values, respectively. The χ^2 still yields an acceptable probability; but in this case the model appears to serve more as an upper limit for the possible quasar influence on the stronger lines, because any further depression in the last bin will only worsen the fit.

This was precisely the effect that was seen when the UVB at the Lyman limit was assumed to be constant with redshift at $J_{\nu_{LL}} = 10^{-21}$ erg cm^{-2} s^{-1} Hz^{-1} sr^{-1} (see Figure 8.4). The comparison here yielded an even higher χ^2 than did the models without any proximity effect whatsoever. There is thus no indication of a proximity effect among the stronger lines in the current spectrum.

The χ^2 values for the fits using the unperturbed Ly α forest, the photoionization model, and the constant value of $J_{\nu_{LL}}$ are all summarized in Table 8.2. The reduced χ^2 is a factor of 10 smaller, because there are 11 bins and because scaling models A1 and A3 beforehand introduced an additional constraint.

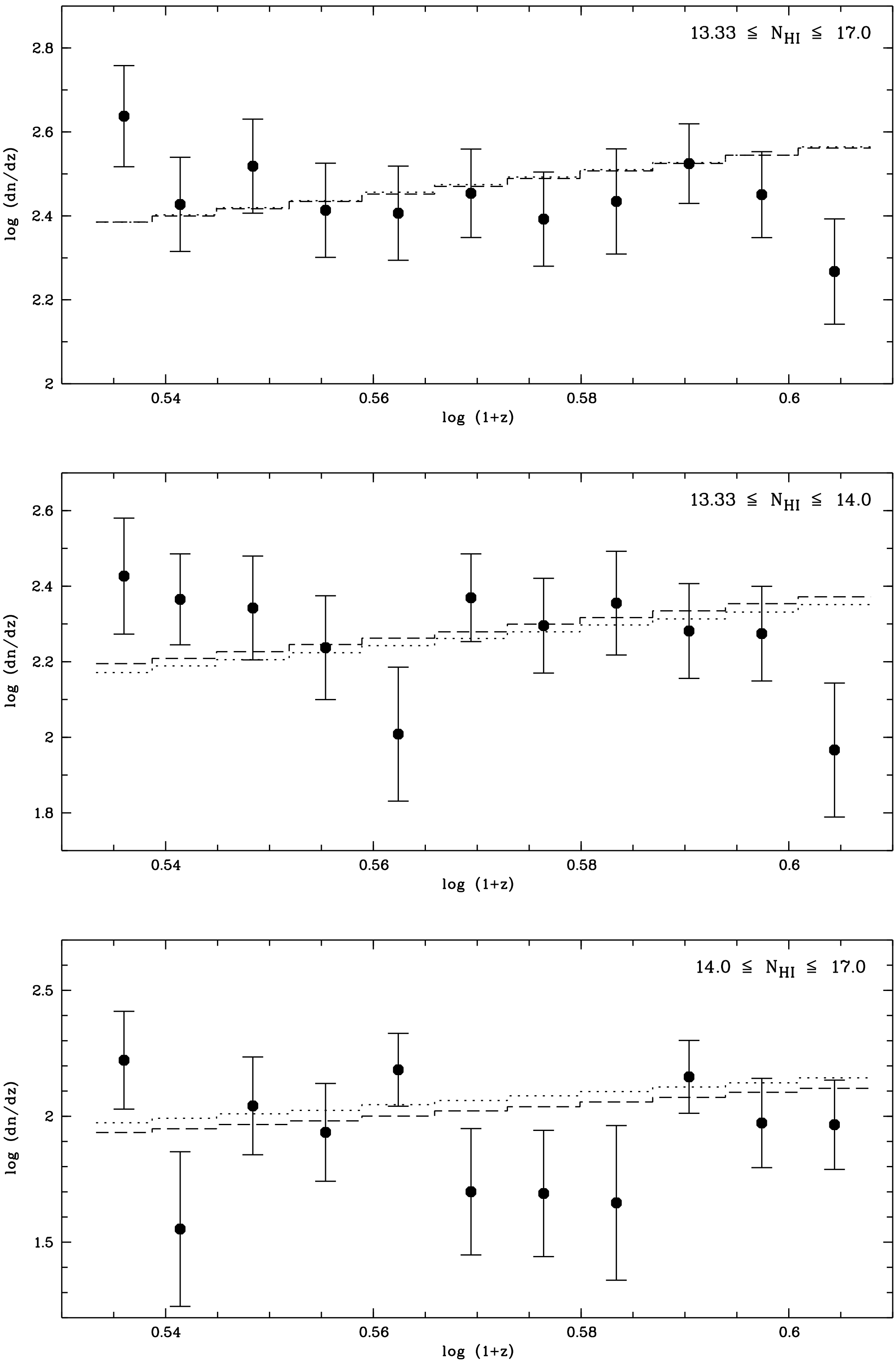

Figure 8.2: *Observed number of lines per unit redshift $d\mathcal{N}/dz$ vs. redshift z for the data, compared to models A1 (dashed line) and A3 (dotted line)* **without any effects of quasar radiation**.

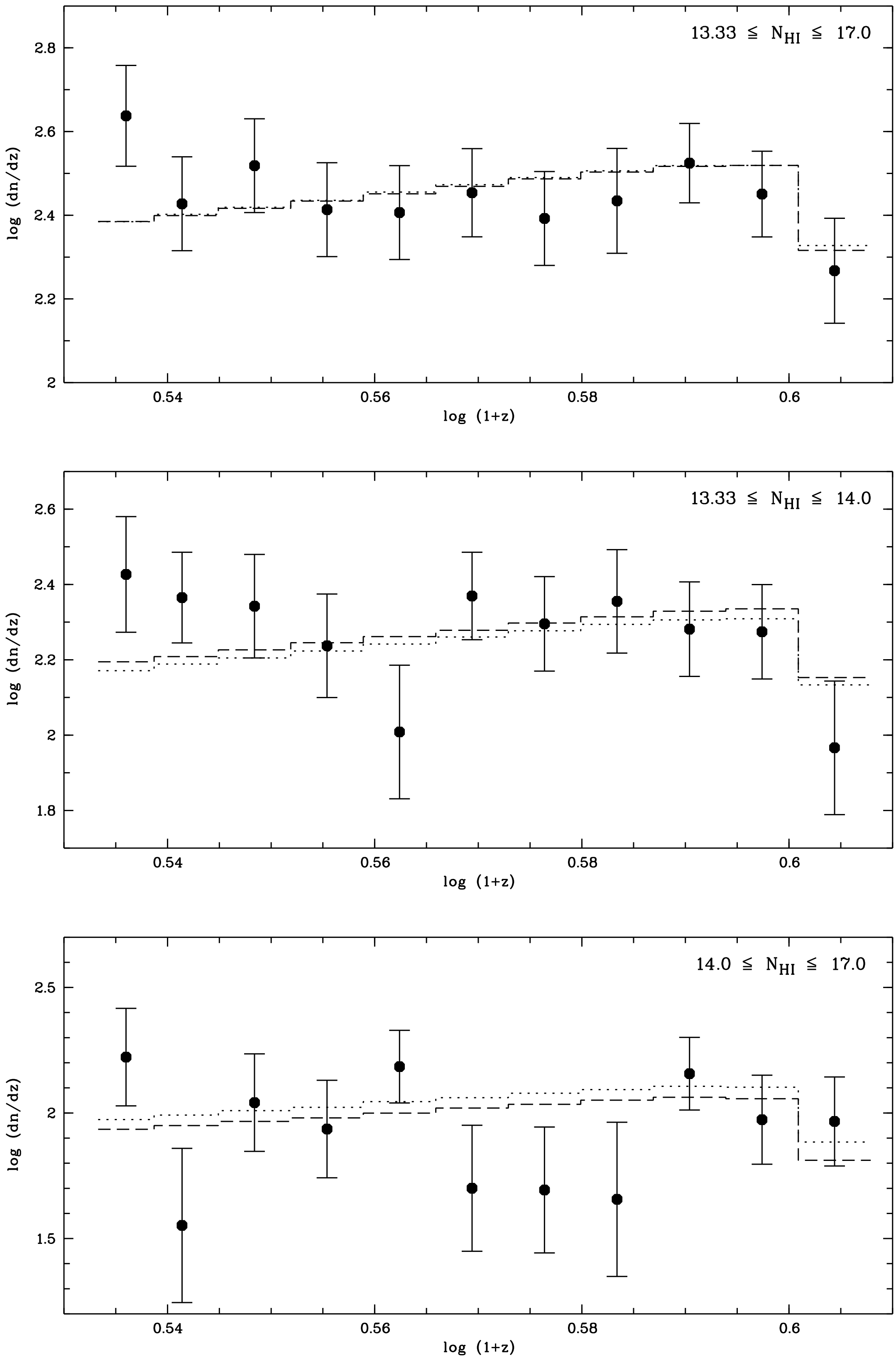

Figure 8.3: *Observed number of lines per unit redshift $d\mathcal{N}/dz$ vs. redshift z for the data, compared to models A1 (dashed line) and A3 (dotted line)* **with UVB "Model I" from Bajtlik, Duncan and Ostriker (1988)**.

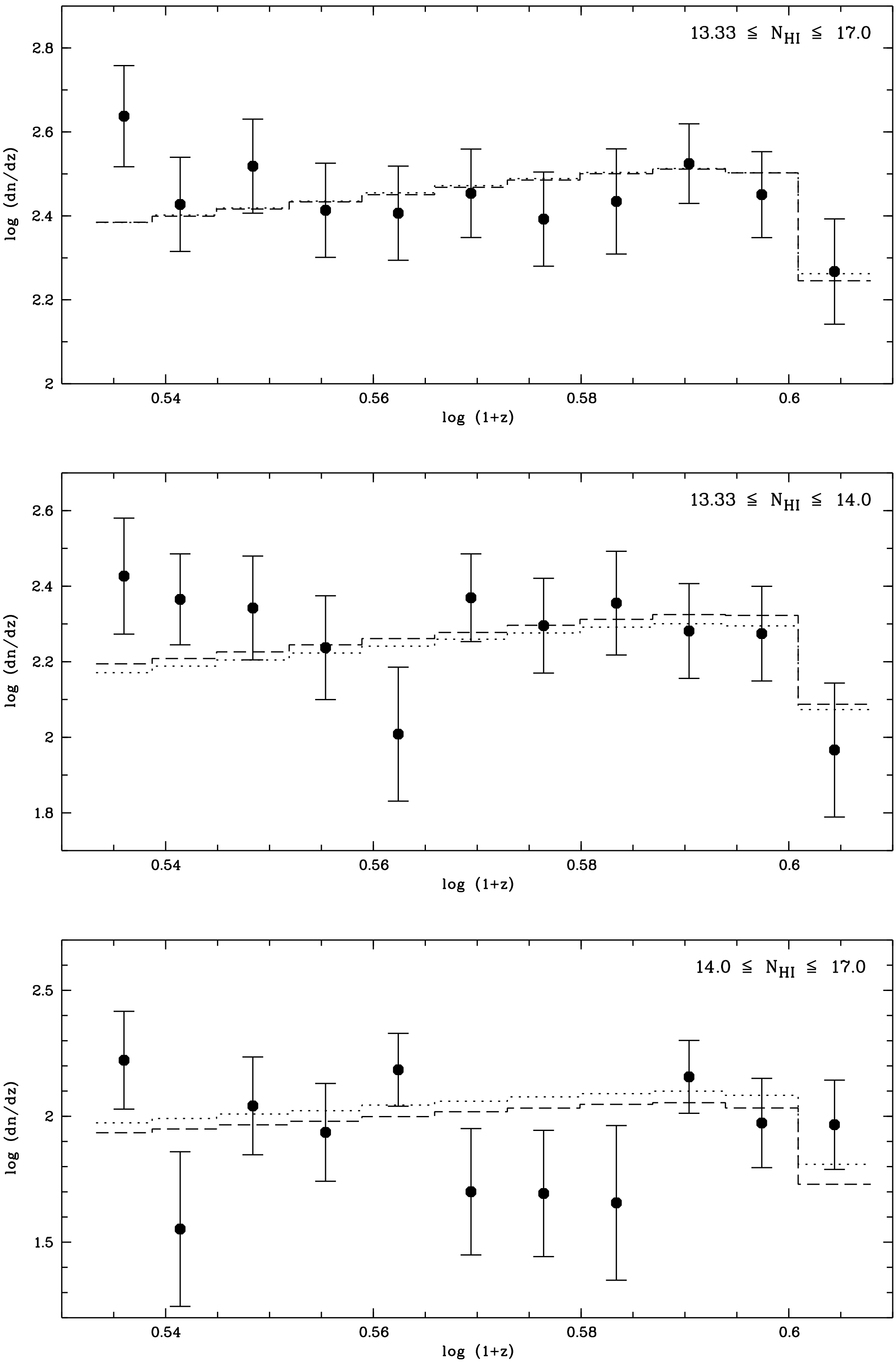

Figure 8.4: *Observed number of lines per unit redshift $d\mathcal{N}/dz$ vs. redshift z for the data, compared to models A1 (dashed line) and A3 (dotted line)* **with $J_{\nu_{LL}} = 10^{-21}$ erg cm^{-2} s^{-1} Hz^{-1} sr^{-1}**.

		$N_{\rm HI} \in [13.33, 17.0]$	$N_{\rm HI} \in [13.33, 14.0]$	$N_{\rm HI} \in [14.0, 17.0]$
no radiation	A1	13.6 (19.2%)	14.0 (17.5%)	13.7 (18.9%)
	A3	13.8 (18.2%)	14.5 (15.1%)	15.0 (13.2%)
BDO model	A1	7.6 (67.1%)	9.3 (50.4%)	13.5 (19.7%)
	A3	7.7 (65.4%)	10.3 (41.6%)	13.7 (18.6%)
$J_\nu = 10^{-21}$	A1	7.2 (70.4%)	8.6 (57.6%)	14.5 (15.3%)
	A3	7.3 (70.0%)	9.7 (46.5%)	14.1 (16.8%)

Table 8.2: *χ^2 and corresponding probabilities (in parentheses) for fits of the Ly α forest with and without quasar radiation.*

Estimate of the UV Background

Finally, to get a better idea of the magnitude of the possible constraints such proximity-effect simulations might have on the UV background, its value J_ν at the Lyman limit was assumed to be merely constant over the entire redshift range from $z = 2.421$ to $z = 3.054$. This constant value was then varied over more than two orders of magnitude to see which values were most compatible with the data, which was now confined to the full sample and the subsample of weaker lines. Following Bechtold (1994), the χ^2 dependence of the fit is plotted in Figure 8.5 and the values are listed in Table 8.3. Model A1 was used for these calculations because it described the data better than model A3 in all but one of the six cases presented in Table 8.2.

Taking the lowest point as the best estimate for the metagalactic ionizing background, this yields a rough approximation of

$$\log J_\nu = -21.0 \pm 0.7 \qquad \text{from } 13.33 \leq N_{\rm HI} \leq 17.0 \tag{8.33}$$

$$\log J_\nu = -21.3 \pm 0.7 \qquad \text{from } 13.33 \leq N_{\rm HI} \leq 14.0 \tag{8.34}$$

at the Lyman limit, which is the order of magnitude that used to be most commonly cited for the proximity effect. Lu, Wolfe and Turnshek (1991) obtained the same value of $\log J_\nu = -21.0 \pm 0.5$ as the original result by Bajtlik, Duncan and Ostriker, but report $\log J_\nu \sim -22.3$ with Keck spectra and a different analysis method at the higher redshift of $z = 4.13$. Although J_ν may decrease at higher redshifts, Giallongo et al. (1996) obtain $J_\nu = (5 \pm 1) \times 10^{-22}$ erg cm^{-2} s^{-1} Hz^{-1} sr^{-1} for $1.7 < z < 4.1$ and argue that earlier values of $\log J_\nu > -21$ resulted because studies with lower resolution and lower S/N than the Keck data assumed a column-density distributions in equation (7.5) that were too steep.

The HE 0940 result above also appears to confirm the assertion by Dobrzycki and Bechtold that the effect is stronger for weaker lines. As mentioned in section 8.7, the photoionization model assumes that the Ly α lines are optically thin; obviously this assumption does not generally hold. Even though smaller lines are much more numerous than saturated ones, many of these are lost in the spectra of all but the highest quality. In any case, a more careful treatment of the ionization-induced proximity effect would need to take curve-of-growth effects into account as well.

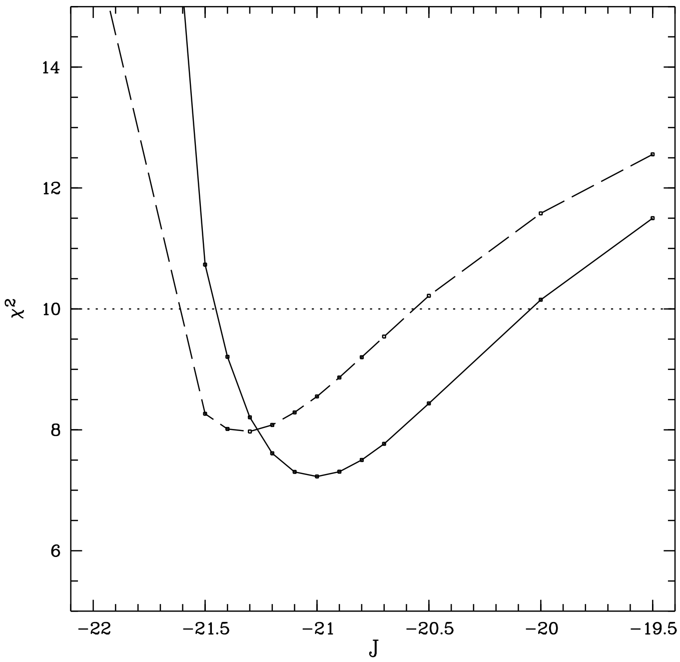

Figure 8.5: χ^2 *vs.* $\log J_{\nu_{LL}}$ *erg cm*^{2} *s*$^{-1}$ *Hz*$^{-1}$ *sr*$^{-1}$ *for the full sample of Ly*α *lines (solid line) and for weaker lines with* $13.33 \leq \log N_{\rm HI} \leq 14.0$ *(dashed line).* $J_{\nu_{LL}}$ *is assumed to be constant with redshift.*

8.7 Proximity-Effect Uncertainties

There are many sources of uncertainties and possible systematic errors involved in the determination of the metagalactic UV background by means of the proximity effect, or more specifically from the ionization model described in section 8.1. Some of the errors have to do with the difficulty of accurately determining the quasar flux density, but others have more to do with the basic assumptions of the model.

Quasar flux density

If no spectrophotometric data is available for the region at or below the observed Lyman limit, extrapolating the quasar flux density to lower wavelengths, as was done in section 8.3, could introduce significant errors. In addition to the errors in the fit itself, the uncertainties in the subjective choice of continuum points could have been further

$\log J_\nu$	χ^2 (full sample)	Q_χ (full sample)	χ^2 (weak lines)	Q_χ (weak lines)
–19.5	11.50	0.32	12.56	0.25
–20.0	10.15	0.43	11.58	0.31
–20.5	8.44	0.59	10.22	0.42
–20.7	7.77	0.65	9.54	0.48
–20.8	7.50	0.68	9.20	0.51
–20.9	7.31	0.70	8.87	0.54
–21.0	7.23	0.70	8.55	0.58
–21.1	7.30	0.70	8.29	0.60
–21.2	7.61	0.67	8.08	0.62
–21.3	8.21	0.61	7.97	0.63
–21.4	9.21	0.51	8.01	0.63
–21.5	10.73	0.38	8.26	0.60
–22.0	33.37	0.00	16.11	0.10

Table 8.3: χ^2 *and corresponding probabilities for fits of* $J_\nu = const.$

biased by the possible presence of weak unresolved emission lines. It appears possible to avoid many of these errors by means of more complicated weighting procedures—developed to measure the H I Gunn-Peterson effect—which use correlations in adjacent pixel fluxes to identify the continuum redward of, and even within, the Ly α forest (Fang et al. 1998). But by far the greatest systematic error in the estimate of the quasar's flux density would result if it turns out that the assumed power law does not describe the quasar continuum well. Though this assumption is widely used, no systematic study or quantitative measure of its validity could be found in the recent literature.

Other authors (Bajtlik, Duncan and Ostriker 1988; Lu, Wolfe and Turnshek 1991) have used the empirical fitting formula (Tytler 1987)

$$\log F_\nu (1 + z_Q)^{-1} = -0.4(m_v - k_v) - 20.09 \tag{8.35}$$

to estimate the observed Lyman-limit flux density F_ν from the quasar's visual magnitude with K-corrections from Evans and Hart (1977). However, in addition to pointing out that these K-corrections do not extend beyond $z = 2.5$, Bechtold (1994) has shown that the resulting F_ν values differ from both the power-law extrapolations and the directly observed Lyman-limit fluxes by more than the error of $\lesssim 40\%$ quoted by Tytler. Instead, this should probably be considered a lower limit for the Lyman-limit flux estimate in general.

As emphasized in section 8.1, one important assumption that is made at the very beginning is that the spectral shape of the ionizing background is the same that of individual quasars. Only then would the ratio of the ionization rates from the UV background and the UV quasar flux equal the ratio of their Lyman-limit flux densities.

But the redshift-dependence of UVB models by Haardt and Madau (1996) and Fardal, Giroux and Shull (1998) exhibits what the latter call “bumps and wiggles” in the background that make this assumption unlikely. Nevertheless, Bechtold (1995) argues that the difference has little effect for “reasonable” spectral energy distributions and estimates the uncertainty introduced to be $\sim 25\%$.

Basic assumptions

The comprehensive list by Bechtold (1995) also includes other systematic effects, which are reiterated only briefly here.

- If the shape of the column-density distribution is flatter than assumed, then J_ν will decrease significantly (Chernomordik and Ozernoy 1993).
- In the unlikely case that the clouds are not as highly ionized as believed, more UV photons from the quasar are needed to produce the observed proximity effect and the actual J_ν is lower than its estimate.
- Similarly, if the absorption lines are saturated rather than optically thin, then the reduction in $N_{\rm HI}$ and thus the ratio of quasar flux to UVB was actually greater than assumed; so the actual J_ν will be lower than its estimate (Chernomordik and Ozernoy 1993).
- If quasars vary on time scales comparable to the $\sim 10^4$ years needed for clouds to reach ionization equilibrium (Bajtlik, Duncan and Ostriker 1988), the observed flux may differ appreciably from the average of the flux responsible for the ionization of the cloud.
- If amplification by gravitational lensing makes quasars appear brighter, then J_ν will also be overestimated.
- If quasars appear dimmer because of dust from intervening galaxies, then the J_ν will also be underestimated.
- If quasar redshifts are systematically higher than assumed, then the actual J_ν has been overestimated (Espey 1993).

Redshift determinations

This last point bears some further discussion because it may radically change the results presented in the previous section. Studies of quasar emission lines (e.g., Gaskell 1982) have shown that the high-ionization lines such as C IV are systematically blueshifted with respect to the lower-ionization lines such as O I and Mg II by an average of roughly 1000 km s^{-1}. Since the C IV “line” at 6280 Å in the 1.52-meter spectrum (Figure 2.1) determined the quasar redshift of $z_{em} = 3.054$ that was used throughout this study, it is quite possible that systematic effects have led to a serious overestimate in the ionizing UV background.

The six absorption lines above 4928.3 Å in the spectrum toward HE 0940 lend further support to this suspicion. The five lines that fall between 4928.3 and 4944 Å are included in Appendices B and C, while the sixth can be seen at 4959 Å in Appendix A. All efforts to identify these lines as metals failed, so assuming they are Ly α lines and using them to estimate the quasar's emission redshift would lead to values of $z = 3.0668$ or $z = 3.0792$, depending on whether the redmost of the group of five or the single line is chosen. The corresponding velocity shifts of 950 km s^{-1} or 1900 km s^{-1} fall well within the range of known values (e.g., Espey et al. 1989).

If the quasar's emission redshift is in fact higher, then the quasar is farther away from the affected Ly α clouds and its sphere of influence is larger than had been assumed. Since a smaller QSO flux produced the observed proximity effect, the influence of the UV background must have been proportionally smaller as well. While the calculations of the preceding section would have to be redone with a higher QSO redshift to determine the exact change in the UVB estimate, it is possible to get an idea of the size of this effect by looking at studies that include a larger sample of quasars. In one such study, Espey (1993) prudently uses each quasar's previous emission-line redshift as the upper limit of the range in which to re-evaluate the proximity effect for a higher QSO redshift. This is important because there is always the danger that the entire proximity effect can be created as a mere artifact of choosing an inaccurately high redshift.

As expected, the results of Espey's study show that an underestimate of the QSO redshift leads to an underestimate of its sphere of influence and an overestimate of the UV background intensity. In his reanalysis of the sample used by Lu et al. (1991), this discrepancy amounted to up to a factor of 6 or 7 for assumed velocity shifts of up to 2500 km s^{-1}. Judging from these results, the UV background in the previous section would have been overestimated by a factor of about 3 to 5, again depending on which of the Ly α lines mentioned above is chosen to be indicative of the "true" emission redshift of HE 0940.

General reflections

As can be seen from the discussion here and the list above, the systematic effects are many; some are difficult to quantify, and several are potentially very large. It is therefore not surprising that, until now, the proximity effect has provided estimates of the UV ionizing background to only within an order of magnitude (which is also the about the size of the greatest discrepancies in current comparisons to theoretical models).

In addition to all of these considerations, the most basic assumption underlying proximity-effect studies of this sort is that the redshift distribution of Ly α absorbers is the same everywhere except when radiation from a nearby quasar leads to greater ionization of the hydrogen and thus to fewer Ly α clouds in that vicinity. But such a decrease need not necessarily stem from enhanced ionization. Some other environmental factors around the quasar may be responsible for the effect instead, for example if quasars exist in high-density environments where velocity dispersions are high (Fernández-Soto et al. 1995) or if neutral gas absorption is suppressed in a high-pressure environment due, e.g., to a nearby supercluster (Rauch et al. 1992, Rauch 1998). Until such alternative explanations can be evaluated or until the large uncertainties listed above can be reduced significantly, it will be difficult to establish whether the proximity effect does indeed measure the UV background intensity. But even as there seems to be a growing awareness that local conditions may play just as large a role, the estimates of the UV background based on the proximity effect seem to be approaching those based on theoretical models of the integrated metagalactic background; the comparison, and the concept of the proximity effect itself, may indeed prove useful.